



Search for Excited and Exotic Electrons in the $e\gamma$ Channel in $p\bar{p}$ Collisions at $\sqrt{s} = 1.96$ TeV

The CDF Collaboration
URL <http://www-cdf.fnal.gov>
(Dated: August 9, 2004)

We present a search for excited and exotic electrons decaying to an electron and a photon with high transverse momentum. We use 200 pb^{-1} of data collected in $p\bar{p}$ collisions at $\sqrt{s} = 1.96$ TeV with the CDF II detector during 2001–2003. No signal above Standard Model expectation is seen in the $ee\gamma$ channel. We discuss the e^* sensitivity in the parameter space of the excited electron mass M_{e^*} and the compositeness energy scale Λ . In the contact interaction model, we exclude $100 < M_{e^*} < 889 \text{ GeV}/c^2$ for $\Lambda = M_{e^*}$. In the gauge-mediated model, we exclude $100 < M_{e^*} < 430 \text{ GeV}/c^2$ for phenomenological coupling $f/\Lambda \approx 10^{-2} \text{ GeV}^{-1}$.

This note describes a search for excited and exotic electrons in $\bar{p}p$ collisions at $\sqrt{s} = 1.96$ TeV with the CDF detector at the Fermilab Tevatron. We search for associated ee^* production followed by the radiative decay $e^* \rightarrow e\gamma$. This mode yields the distinctive $ee\gamma$ final state, which is fully reconstructable with high efficiency and good mass resolution, and has small backgrounds. The evidence for e^* production would be the observation of a narrow resonance in the $e\gamma$ invariant mass distribution.

A. Phenomenology

The Standard Model (SM) of particle physics describes the non-gravitational interactions using the $SU(3)_C \times SU(2)_L \times U(1)_Y$ gauge group. The particle content of the model is given by three generations of quarks and leptons, each containing an $SU(2)_L$ doublet. This fermion multiplicity motivates a description in terms of underlying substructure, in which all quarks and leptons consist of fewer, more elementary particles bound by a new strong interaction [1]. In this compositeness model, quark-antiquark annihilations may result in the production of excited lepton states, such as the excited electron, e^* . The SM gauge group may be embedded in larger gauge groups such as $SO(10)$ or $E(6)$, motivated by grand unified theories or string theory. These embeddings also predict additional, exotic fermions such as the e^* , which can be produced via their gauge interactions [1].

The reaction $q\bar{q} \rightarrow ee^*$ is described in the contact interaction (CI) model by the Lagrangian [1]:

$$L = \frac{4\pi}{\Lambda^2} \bar{q}_L \gamma^\mu q_L \bar{E}_L \gamma_\mu e_L + h.c. \quad (1)$$

where E denotes the e^* field and Λ is the compositeness scale. In the gauge-mediated (GM) model, the Lagrangian describing the e^* coupling to SM gauge fields is [1]:

$$L = \frac{f}{2\Lambda} \bar{E}_R \sigma^{\mu\nu} \left[g \frac{\vec{\tau}}{2} \cdot \vec{W}_{\mu\nu} + g' \frac{Y}{2} B_{\mu\nu} \right] e_L + h.c. \quad (2)$$

leading to the reaction $q\bar{q} \rightarrow Z/\gamma \rightarrow ee^*$. Here $\vec{W}_{\mu\nu}$ and $B_{\mu\nu}$ are the $SU(2)_L$ and $U(1)_Y$ field-strength tensors, g and g' are the corresponding electroweak couplings, and f is a phenomenological parameter.

B. Detector

The detector consists of a magnetic spectrometer with silicon and drift chamber tracking detectors, surrounded by a time-of-flight system, pre-shower detectors, electromagnetic (EM) and hadronic calorimeters, and muon detectors. The main components used in this analysis are the central drift chamber (COT) [7], the central pre-shower detector [8] (for detecting photon conversions), and the central [9] and forward [10] calorimeters. Wire and strip chambers [8] are embedded at the location of the shower-maximum in the central EM calorimeter to measure transverse shower profiles for electron and photon identification. The full acceptance of the COT extends to $|\eta| \sim 1$, where η is the pseudorapidity defined as $\eta = -\ln \tan(\theta/2)$ and θ is the polar angle with respect to the proton beam axis. The central calorimeter covers the region $|\eta| < 1.1$ and the forward calorimeters extend the coverage to $1.1 < |\eta| < 3.5$. The CDF detector is described in detail in [6].

II. DATA SAMPLE & EVENT SELECTION

We use 200 pb⁻¹ of data collected by the CDF II detector [6] during 2001-2003, from $p\bar{p}$ collisions at $\sqrt{s} = 1.96$ TeV at the Fermilab Tevatron. We search for events consisting for two electrons and a photon, all with high transverse energy.

A. Trigger

We trigger on central electron candidates based on high transverse [11] energy (E_T) EM clusters with associated high transverse momentum (p_T) tracks, with an efficiency (governed by the track trigger requirement) of $(96.2 \pm 0.06_{\text{stat}})\%$. We also use a second, less restrictive trigger with a higher E_T threshold, which ensures $\approx 100\%$ trigger efficiency for electrons with $E_T > 100$ GeV.

In the offline analysis, we require fiducial electron and photon candidates with $E_T > 25$ GeV, and the ratio of hadronic to EM energy $E_{\text{Had}}/E_{\text{EM}} < 0.055 + 0.045 \times E/(100 \text{ GeV})$, where E is the EM cluster energy. We also require the isolation $I_{0.4} < 0.1$, where $I_{0.4}$ is the ratio of the calorimeter E_T around the EM cluster within a radius of $R \equiv \sqrt{(\Delta\eta)^2 + (\Delta\phi)^2} = 0.4$, to the cluster E_T . Lateral shower profiles are required to be consistent with test-beam data.

Central electrons are identified by requiring a matching COT track, while central photons have a veto on a matching COT track with $p_T > (1 + 0.005 \times E_T/\text{GeV}) \text{ GeV}/c$. Photon background from π^0/η decays is suppressed by vetoing events with a second cluster in the same shower-maximum strip chamber of the EM calorimeter. The longitudinal position of the electron track at the beamline (z_{vertex}) is required to be within 60 cm of the center of the detector. Forward electrons and photons are not distinguished by using tracking information (in order to maximize selection efficiency), but are collectively identified as forward EM objects. We select forward EM objects in the range $1.2 < |\eta| < 2.8$, with the same $E_{\text{Had}}/E_{\text{EM}}$ and $I_{0.4}$ requirements as central candidates, and demand consistency of the 2-D lateral shower profile with test-beam data. Finally, events with dielectron invariant mass in the range $81 < m_{ee} < 101 \text{ GeV}/c^2$ are rejected to suppress $Z(\rightarrow ee)\gamma$ background.

C. Energy Scale and Resolution

We calibrate the EM energy response by requiring the measured $Z \rightarrow ee$ boson mass to agree with the current world average [13]. The simulated resolution is tuned using the observed width of the mass peak.

III. SIGNAL ACCEPTANCE

A. EM Object Identification Efficiencies

Offline identification efficiencies for EM objects are measured using an unbiased “probe” electron from $Z \rightarrow ee$ events which are triggered and identified using the other electron. The same procedure is applied to a GEANT[12]-based detector simulation of $Z \rightarrow ee$ events. We find good agreement between data and simulation for the measured efficiency of electrons.

The simulation of photons is validated by using the probe electron to emulate a photon, with and without a prior selection ($0.9 < E_T/p_T < 1.1$) to suppress bremsstrahlung from the probe electron. These comparisons confirm that the simulation reproduces the calorimetric and tracking cut efficiencies for photon-like objects, and we assign a systematic uncertainty on the central photon efficiency predicted by the simulation due to any differences.

The efficiency for forward EM objects was measured using central-forward $Z \rightarrow ee$ events that are triggered and identified using the central electron. Simulation and data confirm that the inefficiency (due to extraneous soft energy near the forward EM object) decreases with increasing EM object E_T , falling below 1% for $E_T > 100 \text{ GeV}$.

B. Total Signal Acceptance

We calculate the full acceptance (including geometric, kinematic and identification cuts) using the detector simulation. We generate $ee^* \rightarrow ee\gamma$ events using PYTHIA [14] for the CI model, and the LANHEP [15] and COMPHEP [16] programs for the GM model. We calculate the acceptance as a function of M_{e^*} for each model separately, and find that it rises from 15% at $M_{e^*} = 100 \text{ GeV}/c^2$ to 33% asymptotically at high mass. The largest difference in acceptance between the two models is about 5% at $M_{e^*} = 200 \text{ GeV}/c^2$. The systematic uncertainties on the acceptance come from identification efficiency, simulation of passive material, parton distribution functions (PDFs), trigger efficiency, $|z_{\text{vertex}}| < 60 \text{ cm}$ cut, and energy scale and resolution.

IV. BACKGROUNDS

Sources of background, in order of decreasing contribution, are production of (1) $Z\gamma \rightarrow ee\gamma$, (2) $Z + \text{jet} \rightarrow ee\gamma$ where the jet is mis-identified as a photon, (3) $WZ \rightarrow eee\nu$ and $ZZ \rightarrow eeee$ where an electron is identified as a photon, (4) multi-jet events where jets are mis-identified as electrons and photons, (5) $t(\rightarrow e\nu b)\bar{t}(\rightarrow e\nu\bar{b})$ with hard

TABLE I: Comparison of integrated backgrounds and signal candidates above a given mass cut, for various kinematic quantities.

$M_{e\gamma}$			$M_{ee\gamma}$		
mass cut	backgrounds	data	mass cut	backgrounds	data
$> 0 \text{ GeV}/c^2$	$6.5^{+0.9}_{-0.6}$	7	$> 0 \text{ GeV}/c^2$	$3.0^{+0.4}_{-0.3}$	3
$> 80 \text{ GeV}/c^2$	$3.1^{+0.6}_{-0.3}$	5	$> 80 \text{ GeV}/c^2$	$2.7^{+0.5}_{-0.4}$	3
$> 150 \text{ GeV}/c^2$	$0.8^{+0.2}_{-0.1}$	3	$> 150 \text{ GeV}/c^2$	$1.6^{+0.3}_{-0.2}$	3
$> 225 \text{ GeV}/c^2$	$0.2^{+0.07}_{-0.04}$	1	$> 225 \text{ GeV}/c^2$	$0.6^{+0.2}_{-0.1}$	2
$> 250 \text{ GeV}/c^2$	$0.1^{+0.02}_{-0.01}$	1	$> 250 \text{ GeV}/c^2$	0.4 ± 0.1	2
$> 300 \text{ GeV}/c^2$	$0.04^{+0.02}_{-0.01}$	0	$> 300 \text{ GeV}/c^2$	$0.17^{+0.06}_{-0.04}$	2
$> 350 \text{ GeV}/c^2$	$0.015^{+0.008}_{-0.004}$	0	$> 350 \text{ GeV}/c^2$	$0.07^{+0.03}_{-0.02}$	0

photon radiation off the daughter b quarks, (6) diphoton+jet events, and (7) $W(\rightarrow e\nu) + 2$ jets where the jets are mis-identified as an electron and a photon.

We estimate the $Z\gamma$, WZ , ZZ , $t\bar{t}$ and diphoton+jet backgrounds using the simulation, using the ZGAMMA [18] generator for the $Z\gamma$ process and PYTHIA for the others. Uncertainties in these background predictions are due to integrated luminosity (6%) [19], PDFs uncertainties on acceptance, higher order QCD corrections to leading order cross sections, identification efficiencies, simulation of passive material, and energy scale and resolution.

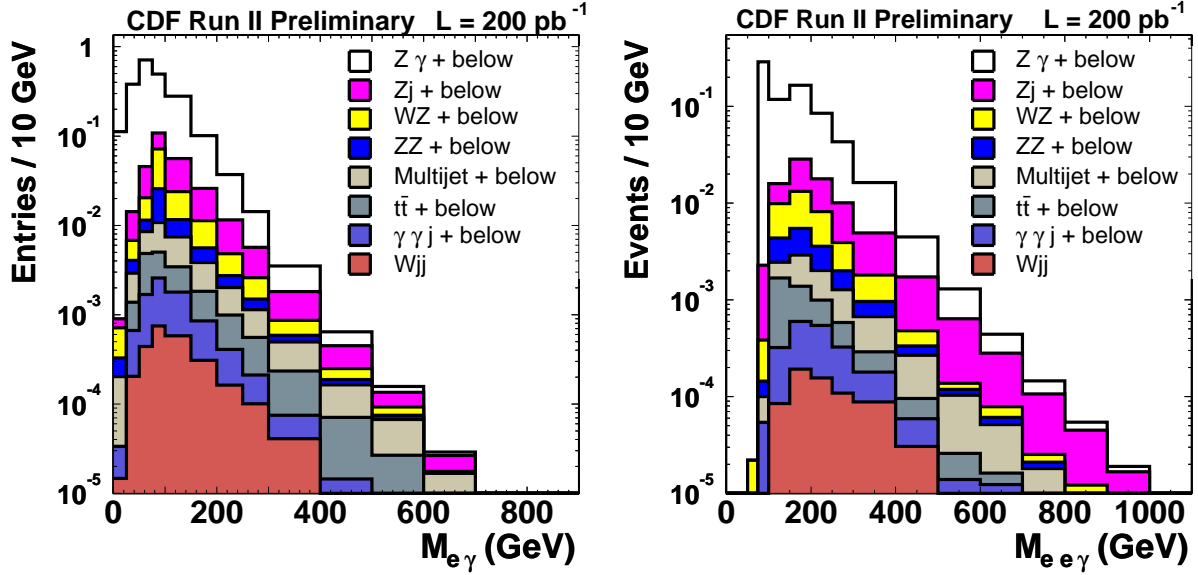


FIG. 1: Left: The cumulative $e\gamma$ mass distribution for all backgrounds. Integrating over all masses, the total expected number of $e\gamma$ entries is 6.47 ± 0.12 (stat) $^{+0.82}_{-0.58}$ (syst). Right: cumulative $ee\gamma$ mass distribution for all backgrounds. Integrating over all masses, the total expected number of $ee\gamma$ entries is 3.01 ± 0.08 (stat) $^{+0.38}_{-0.27}$ (syst).

Backgrounds from Z +jet, W +2 jet and multi-jet sources are estimated using data samples of such events, weighted by the appropriate rates for jets to be misidentified as electrons and photons. These “fake” rates are measured using jet-triggered data and electron-triggered data, excluding W and Z boson candidates. The photon fake rate is corrected for the prompt photon fraction in the jet sample, which is estimated using the rate of conversion signals in the calorimeter pre-shower detector. All fake rates are applied as functions of E_T .

V. CANDIDATE EVENTS

We find three candidate events, consistent with our total background prediction of 3.01 ± 0.08 (stat) $^{+0.4}_{-0.3}$ (syst). The systematic uncertainty receives approximately equal contributions from the uncertainty on the SM backgrounds and the uncertainty on the mis-identification backgrounds due to the fake rates. Comparisons of integrated backgrounds and signal candidates above a given mass cut are shown in Table I and Figure 2. The kinematics of the candidates are

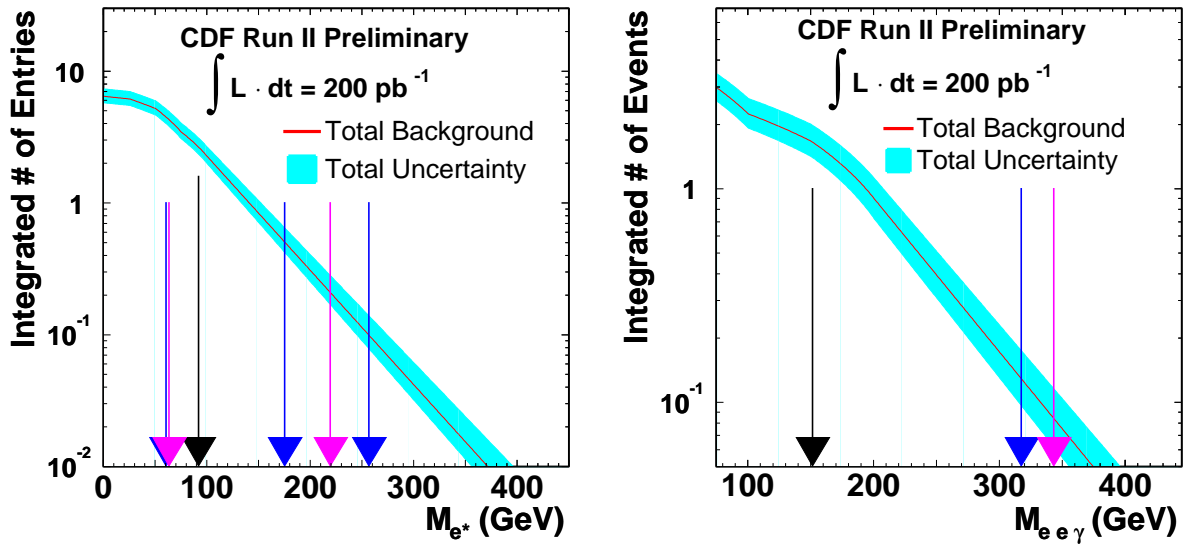


FIG. 2: The left figure shows the integrated background prediction from high mass to low mass for the M_{e^*} distribution. The right figure shows the integrated background prediction from high mass to low mass for the $M_{ee\gamma}$ distribution. The observed events are overlaid in black for Run=147806 Event=1167222 (event 2), blue for Run=144674 Event=4143240 (event 1), and magenta for Run=167866 Event=443088 (event 3).

TABLE II: Kinematics of the candidate events. e, γ and j represent electron, photon and jet respectively. For forward EM objects, e and γ designations serve as distinguishing labels only. Electron charge information is indicated when available.

kinematic	event 1	event 2	event 3
$E_T(e_1)$	37 GeV	44 GeV	164 GeV
$E_T(e_2)$	71 GeV	42 GeV	94 GeV
$E_T(\gamma)$	48 GeV	46 GeV	72 GeV
$\eta(e_1)$	-1.01	0.83	-0.03
$\eta(e_2)$	1.27	-0.17	0.46
$\eta(\gamma)$	-1.64	1.47	-0.29
$m(e_1 e_2)$	176 GeV/ c^2	78 GeV/ c^2	256 GeV/ c^2
$m(e_1 \gamma)$	61 GeV/ c^2	92 GeV/ c^2	219 GeV/ c^2
$m(e_2 \gamma)$	257 GeV/ c^2	92 GeV/ c^2	64 GeV/ c^2
$m(e_1 e_2 \gamma)$	318 GeV/ c^2	152 GeV/ c^2	343 GeV/ c^2
$E_T(j)$		26 GeV	
$\eta(j)$		1.53	
$m(e_2 j)$		92 GeV/ c^2	

presented in Table II. Event 2 has an additional jet that passes forward selection cuts but marginally fails the isolation cut ($I_{0.4} = 0.107$). Both forward objects have associated tracks in the silicon detector and are consistent with being electrons. One pair of dielectron invariant mass combinations is consistent with the event being a $Z(\rightarrow ee)Z(\rightarrow ee)$ candidate.

VI. RESULTS

For the e^* resonance search, we compare the data with the expected background in a sliding window of $\pm 3\sigma$ width on the $e\gamma$ invariant mass distribution, where σ is the RMS of the observable mass peak. For each event, all possible $e\gamma$ combinations are considered. The RMS is dominated by the detector resolution ($\sim 3.5\%$) over almost the entire parameter space of the e^* models. Figure 1 shows the background predictions from all sources for $e\gamma$ combinations.

We set limits on e^* production using a Bayesian [13, 20] approach, with a flat prior for the signal and Gaussian priors for the acceptance and background uncertainties. The 95% confidence level (C.L.) cross section upper limits (see Fig. 3) are converted into e^* mass limits by comparing them to the theoretical cross sections (LO calculations

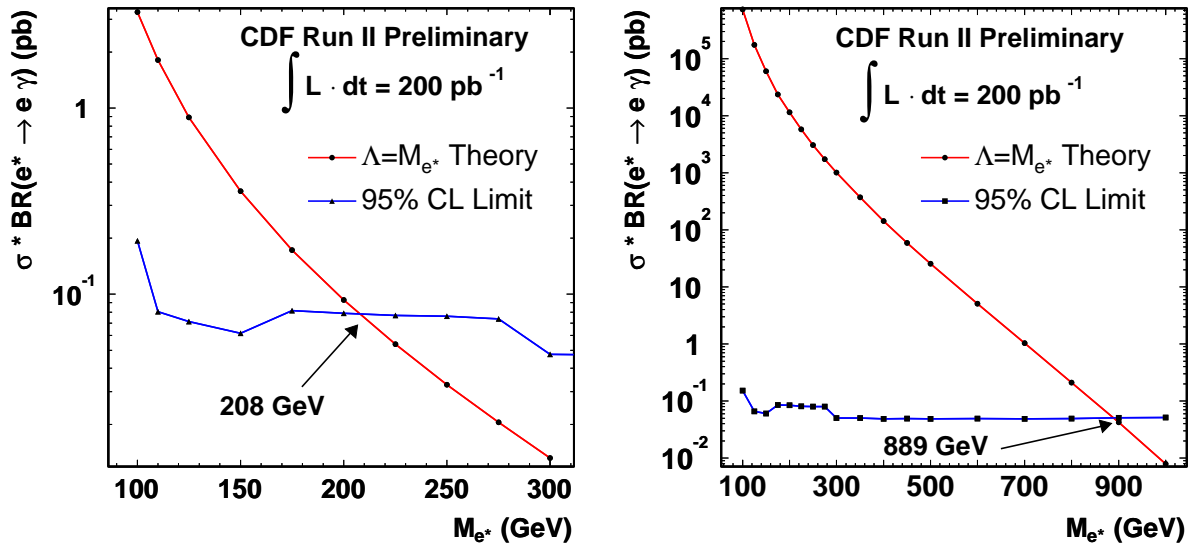


FIG. 3: The experimental cross section limits for the GM (left) and CI (right) models, compared to the respective theoretical cross sections for $M_{e^*} = \Lambda$.

reweighted by a multiplicative next-to-leading order QCD K -factor, 1.3%). Figure 4 shows the limits in the parameter space of f/Λ vs M_{e^*} for the GM model, and M_{e^*}/Λ vs M_{e^*} for the CI model. The region above the curve labeled “ $\Gamma_{e^*} = 2M_{e^*}$ ” is unphysical for the GM model, because the total decay width of the e^* becomes much larger than its mass.

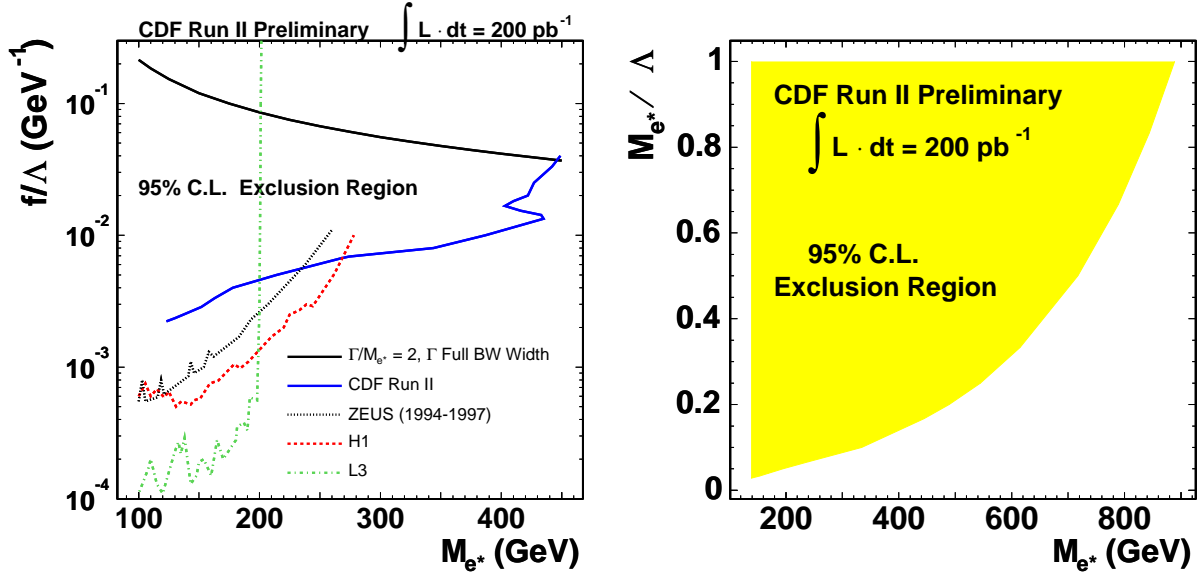


FIG. 4: The 2-D parameter space regions excluded by this analysis for the GM model (top) and the CI model (bottom), along with the current world limits.

In conclusion, we have presented the results of the first search for excited or exotic electrons at a hadron collider. We find three candidate events, consistent with our total background prediction. In the gauge-mediated model, we exclude $M_{e^*} < 430 \text{ GeV}/c^2$ for $f/\Lambda \sim 0.01 \text{ GeV}^{-1}$ at the 95% C.L., well beyond previous limits [2–5]. We have also presented the first e^* limits in the contact interaction model as a function of M_{e^*} and Λ , excluding $100 < M_{e^*} < 889 \text{ GeV}/c^2$ for $M_{e^*} = \Lambda$.

Acknowledgments

We thank the Fermilab staff and the technical staffs of the participating institutions for their vital contributions. This work was supported by the U.S. Department of Energy and National Science Foundation; the Italian Istituto Nazionale di Fisica Nucleare; the Ministry of Education, Culture, Sports, Science and Technology of Japan; the Natural Sciences and Engineering Research Council of Canada; the National Science Council of the Republic of China; the Swiss National Science Foundation; the A.P. Sloan Foundation; the Bundesministerium fuer Bildung und Forschung, Germany; the Korean Science and Engineering Foundation and the Korean Research Foundation; the Particle Physics and Astronomy Research Council and the Royal Society, UK; the Russian Foundation for Basic Research; the Comision Interministerial de Ciencia y Tecnologia, Spain; and in part by the European Community's Human Potential Programme under contract HPRN-CT-20002, Probe for New Physics.

-
- [1] U. Baur, M. Spira and P. M. Zerwas, Phys. Rev. D **42**, 815 (1990), and references therein; E. Boos *et al.*, Phys. Rev. D **66**, 013011 (2002), and references therein.
 - [2] ZEUS Collaboration, S. Chekanov *et al.*, Phys. Lett. B **549**, 32 (2002).
 - [3] H1 Collaboration, C. Adloff *et al.*, Phys. Lett. B **548**, 35 (2002).
 - [4] ALEPH Collaboration, D. Buskulic *et al.*, Phys. Lett. B **385**, 445 (1996); DELPHI Collaboration, P. Abreu *et al.*, Eur. Phys. J. C **8**, 41 (1999); L3 Collaboration, P. Achard *et al.*, Phys. Lett. B **568**, 23 (2003).
 - [5] OPAL Collaboration, G. Abbiendi *et al.*, Phys. Lett. B **544**, 57 (2002).
 - [6] T. Affolder *et al.*, FERMILAB-Pub-96/390-E.
 - [7] T. Affolder *et al.*, Fermilab-Pub-03-355-E (accepted for publication in Nucl. Instrum. Meth. Phys. Res. A).
 - [8] A. Byon-Wagner *et al.*, IEEE Trans. Nucl. Sci **49**, 2567 (2002).
 - [9] CDF Collaboration, F. Abe *et al.*, Nucl. Instrum. Methods Phys. Res. A **271**, 387 (1988); D. Amidei *et al.*, Nucl. Instrum. Methods Phys. Res. A **350**, 73 (1994).
 - [10] CDF Collaboration, F. Abe *et al.*, Nucl. Instrum. Methods Phys. Res. A **271**, 387 (1988); D. Amidei *et al.*, Nucl. Instrum. Methods Phys. Res. A **350**, 73 (1994).
 - [11] “Transverse” energy and momentum imply the respective components perpendicular to the beam axis.
 - [12] R. Brun and F. Carminati, CERN Program Library Long Writeup, W5013, 1993 (unpublished), version 3.15.
 - [13] K. Hagiwara *et al.*, Phys. Rev. D **66**, 010001 (2002).
 - [14] T. Sjöstrand, Comput. Phys. Commun. **82**, 74 (1994), version 6.127.
 - [15] A. V. Semenov, hep-ph/0208011 (2002); A. V. Semenov, Comput. Phys. Commun. **115**, 124 (1998).
 - [16] A. Pukhov *et al.*, hep-ph/9908288 (1999); E. E. Boos *et al.*, hep-ph/9503280 (1995).
 - [17] J. Pumplin *et al.*, JHEP **07**, 012 (2002).
 - [18] U. Baur and E. Berger, Phys. Rev. D **47**, 4889 (1993).
 - [19] S. Klimenko, J. Konigsberg, and T. M. Liss, Fermilab-FN-0741, December 2003 (unpublished).
 - [20] I. Bertram *et al.*, Fermilab-TM-2104, April 2000 (unpublished).